



# CeO<sub>2-x</sub> platelet from monometallic cerium layered double hydroxides and its photocatalytic reduction of CO<sub>2</sub>



Ting Ye <sup>a,b</sup>, Weimin Huang <sup>a,\*</sup>, Liming Zeng <sup>a,b</sup>, Mengli Li <sup>a,b</sup>, Jianlin Shi <sup>a,\*</sup>

<sup>a</sup> State Key Lab of High Performance Ceramics and Superfine Microstructure, Shanghai Institute of Ceramics, Chinese Academy of Sciences, 1295 Dingxi Road, Shanghai, 200050, PR China

<sup>b</sup> University of Chinese Academy of Sciences, 19 Yu-quan Road, Beijing, 100049, PR China

## ARTICLE INFO

### Article history:

Received 21 December 2016

Received in revised form 10 March 2017

Accepted 20 March 2017

Available online 22 March 2017

### Keywords:

Monometallic cerium layered double hydroxides

Cerium oxide platelets

CO<sub>2</sub> photoreduction

## ABSTRACT

Monometallic cerium layered double hydroxides (M Ce-LDHs) were successfully synthesized for the first time through a simple approach. XRD, TEM, SEM, XPS, FT-IR, TG-DSC techniques and UV-vis diffuse reflectance spectroscopy were used to characterize the samples. The obtained M Ce-LDHs showed typical layered structure composing of quasi-hexagonal platelets with side length of about 2  $\mu$ m and thickness about tens of nanometers, and preserved its platelet morphology after heat treatment at up to 800 °C. Our study also revealed that the heat-treatments at different temperatures could be employed to tune the concentration ratio of Ce<sup>3+</sup>/Ce<sup>4+</sup> and the surface area of those cerium oxide platelets, both of which play a key role in the photocatalytic activity towards photoreduction of CO<sub>2</sub>.

© 2017 Elsevier B.V. All rights reserved.

## 1. Introduction

Cerium-based materials have been extensively studied owing to their unique redox capability, high activity of reaction and capability of oxygen storage-and-release, which play crucial roles in many fields, such as three-way catalytic conversion of automobile gasoline engine exhausts [1–3], CO oxidation [4–6], methanol steam reforming [7,8] and water-gas shift [9,10]. The high catalytic activity of cerium-based materials is related to their structural properties, such as lattice structure, low dimensional nanostructure, distributions of oxygen vacancies and catalytic active sites, in addition to its bulk composition [11]. Therefore, finding of novel and special material structures may give rise to unprecedented material properties, e.g., specific catalytic functionalities.

Layered double hydroxides (LDHs) are known as a kind of ionic lamellar compounds comprising of positive-charged host layers and exchangeable interlayer anions [12]. LDHs have been of particular interest due to their structural properties of such as the tailored chemical composition of both host layers and interlayer anions, the high dispersion of active sites, and easy modulation of the active center structures (e.g., crystal facets, defects) at atomic scale [13]. These structural characteristics make LDHs promising mate-

rial systems for the fabrication of novel catalysts. What interested us most is to develop a novel 2D layered monometallic cerium-based catalyst which would display multi-facet advantages in both the LDH structure and the intrinsic catalytic activities of cerium-based materials. As far as we know, the synthesis of monometallic cerium LDHs have not been reported in previous literatures.

In fact, it has long been desired to develop monometallic rare earth LDHs. Recently, layered rare earth hydroxide (LREHs) compounds comprising of cationic rare earth hydroxide layers and intercalated anions have been synthesized by several groups [14–16]. LREH compounds of most of lanthanide series have been synthesized by a homogeneous alkalinization route [17–19]. However, there are still difficulties in synthesizing monometallic cerium layered double hydroxides, probably due to the different electronic structure of cerium from other lanthanide ions. Only one-dimensional nanowires or nanorods have been obtained by using conventional synthetic methods [17].

Herein, we demonstrate a simple approach toward the synthesis of monometallic cerium layered double hydroxides. The key to obtain monometallic cerium LDH lies in the use of ammonium persulfate during the conventional homogeneous alkalinization process. Ammonium persulfate was ever used as oxidant to synthesize Ni<sup>2+</sup>-Mn<sup>3+</sup>-LDHs [20]. In our case, ammonium persulfate plays a key role in synthesis of layered monometallic cerium based material through the oxidation of partial Ce<sup>3+</sup> into Ce<sup>4+</sup>. The as-synthesized Ce<sup>3+</sup>Ce<sup>4+</sup>-LDHs (M Ce-LDHs) showed a well-defined crystalline structure and uniform layered morphology. Their struc-

\* Corresponding authors.

E-mail addresses: [huangwm706@mail.sic.ac.cn](mailto:huangwm706@mail.sic.ac.cn) (W. Huang), [jishi@mail.sic.ac.cn](mailto:jishi@mail.sic.ac.cn) (J. Shi).

tural features will be discussed on the basis of Fourier transform infrared (FT-IR) spectra and thermal behavior as well as X-ray diffraction (XRD) data, and the influences of calcination temperature on its photocatalytic activity will also be investigated.

## 2. Experimental

### 2.1. Synthesis procedure

All the chemicals were analytical grade and used as received without further purification. Monometallic cerium layered double hydroxides ( $\text{Ce}^{3+}\text{Ce}^{4+}$ -LDHs) were synthesized by a renewed homogeneous alkalization route. Briefly,  $\text{Ce}(\text{NO}_3)_3 \cdot 6\text{H}_2\text{O}$  (1 mmol),  $\text{NaCl}$  (13 mmol), hexamethylenetetramine (HMT) (5 mmol) and  $(\text{NH}_4)_2\text{S}_2\text{O}_8$  (0–1.5 mmol) were dissolved in 200 mL of water to produce a clear solution. The resulting solution was refluxed under Argon protection for 20 h. The precipitate was then formed, filtered and washed with deionized water and ethanol in turns before being dried in air at room temperature. Moreover, The as-synthesized  $\text{Ce}^{3+}\text{Ce}^{4+}$ -LDHs were calcined at 400 °C, 600 °C, 800 °C and 1000 °C for 6 h in air to study the influences of calcination temperature on its photocatalytic activity. The calcined products were denoted as  $\text{MCe-LDH-x}$ , where x represents the calcination temperature.

### 2.2. Chemical analysis

The content of cerium in the prepared material was determined by inductively coupled plasma (ICP) atomic emission spectroscopy on an Agilent 725 spectrometer. The  $\text{Ce}^{4+}$  content was determined with iodometric titrations reported by Pierre Vialat [21], and anions were analyzed by ion chromatography (ICS-2100). For the determination of  $\text{OH}^-$ , synthesized sample (approximately 0.1 g) was dissolved in 17  $\text{cm}^3$  of standard HCl solution (0.11 M) and then back-titrated with standard NaOH solution (0.15 M) under the monitoring by a pH meter. The pH value of the solution was plotted against the volume of NaOH solution added to identify the titration end point [19]. Water content was determined by thermogravimetric differential thermal analysis (TG-DTA) using a Netzsch STA449C instrument in air in the temperature range 25–800 °C with a linear temperature ramp of 5 °C per min.

### 2.3. Characterization

The X-ray powder diffraction (XRD) was conducted on a Rigaku D/Max 2200PC diffractometer with  $\text{CuK}\alpha$  radiation ( $\lambda = 0.15405 \text{ nm}$ ) and operated at 40 mA and 40 kV with a scanning rate of 4° per min. Morphological and compositional analysis of the synthesized samples were made on a HI-TACHI SU8220 SEM under an operating voltage of 1 kV, and a JEOL-2010F transmission electron micro-scope (TEM) spectrometer at 200 kV. The specific surface area of the synthesized samples were determined by an  $\text{N}_2$  physisorption and desorption method using a Tristar 3000 BET analyzer at 77 K. Fourier transform infrared (FT-IR) spectra were recorded within a range of 400–4000  $\text{cm}^{-1}$  using KBr pellets on a Varian 3100 FT-IR spectrometer. The surface information and cerium valence state ( $\text{Ce}^{3+}$  and  $\text{Ce}^{4+}$ ) analysis were detected by X-ray photoelectron spectroscopy (XPS ESCALAB 250). Ultraviolet visible (UV-vis) absorption spectra were recorded by UV-3101PC Shimadzu spectroscope from the scale range of 200–800 nm.

### 2.4. Photocatalytic activity evaluation

Photocatalytic activity tests for the reduction of  $\text{CO}_2$  with  $\text{H}_2\text{O}$  were performed in a gas-closed photoreactor with the volume of 500 mL as reported previously [22]. Typically, 50 mg photocatalyst was uniformly dispersed on a glass plate (2.5 cm × 2.5 cm) which

**Table 1**  
Elemental Analysis Results on  $\text{MCe-LDH}$ .

Element analysis	$\text{Ce}^{3+}$	$\text{Ce}^{4+}$	$\text{SO}_4^{2-}$	$\text{NO}_3^-$	OH	$\text{H}_2\text{O}$
Content (%)	25.70	27.35	21.89	3.96	13.60	7.50
Chemical Formula	$\text{Ce}_{0.98}^{4+}\text{Ce}_{0.92}^{3+}(\text{OH}^-)_{4.00}(\text{NO}_3^-)_{0.32}(\text{SO}_4^{2-})_{1.14} \cdot 2.08\text{H}_2\text{O}$					

was fixed in the center of reactor. Prior to irradiation, high purity  $\text{CO}_2$  (99.99%) gas, monitored by a mass flow controller, was bubbled through deionized water for 20 min to generate a mixture of  $\text{CO}_2$  and water vapor, and then the reactor was tightly closed and kept in the  $\text{CO}_2$ - $\text{H}_2\text{O}$  atmosphere for at least 30 min to ensure the adsorption-desorption balance. After that, a xenon lamp (300 W) was put at the top of quartz window with the distance of 1 cm, which can irradiate the whole catalyst powder. The photocatalytic  $\text{CO}_2$  reduction with  $\text{H}_2\text{O}$  was performed for 8 h in each run and the reaction temperature was maintained at 25 °C by cooling water circulation. During the irradiation, 1 mL gas was sampled from the glass chamber every one hour for analyzing the reaction products. In this work, the carbonous products were analyzed by a gas chromatograph (GC-2060, Fuli Corp., China) with a flame ionization detector (FID) equipped with a 5A molecular column and a TDX-01 packed column and the evolved  $\text{H}_2$  and  $\text{O}_2$  gases were analyzed by a gas chromatography (GC7900, Techcomp) with a thermal conductive detector (TCD) equipped with a 5A molecular sieve column.

As for the stability test of photocatalytic activity, the photocatalyst was collected after each run and then heat-treated at 150 °C for two hours before reusing for photoreduction of  $\text{CO}_2$ .

Blank experiments were also performed to ensure the elimination of surrounding interferences. And these experiments were conducted at the following conditions: (1) dark experiment with the catalyst and  $\text{CO}_2$ , (2) light irradiation with  $\text{CO}_2$  in the absence of catalyst, and (3) using  $\text{N}_2$  instead of  $\text{CO}_2$  under the same experimental conditions. No products were detected in these reactions.

## 3. Results and discussion

### 3.1. Characterization of the as-prepared samples

The material synthesis was started by dissolving  $\text{Ce}(\text{NO}_3)_3 \cdot 6\text{H}_2\text{O}$ ,  $\text{NaCl}$ , HMT and  $(\text{NH}_4)_2\text{S}_2\text{O}_8$  in water, followed by refluxing the mixture solution under Argon protection for 20 h. A white precipitate was formed after refluxing for about 1 h, which was continued for further promoted crystallization. In this work, we chose the optimal molar ratio of  $(\text{NH}_4)_2\text{S}_2\text{O}_8/\text{Ce}(\text{NO}_3)_3$  at 0.6 for the follow-up investigations and the detailed optimization of  $(\text{NH}_4)_2\text{S}_2\text{O}_8/\text{Ce}(\text{NO}_3)_3$  molar ratio was shown in the Supporting information (SI-1).

On the basis of chemical analysis results (Table 1), the chemical composition of the as-obtained sample could be determined to be  $\text{Ce}_{0.98}^{4+}\text{Ce}_{0.92}^{3+}(\text{OH}^-)_{4.00}(\text{NO}_3^-)_{0.32}(\text{SO}_4^{2-})_{1.14} \cdot 2.08\text{H}_2\text{O}$ .

XRD pattern of the as-obtained sample (Fig. 1a) shows sharp diffraction peaks with d-spacing values of 0.838 and 0.419 nm in a low-angle region, being characteristic of a typical layered structure. SEM observation of the product reveals that the as-obtained sample is composed of quasi-hexagonal platelets with side length of about 2  $\mu\text{m}$  and thickness about tens of nanometers (Fig. 1b). TEM image of the product shows an angle of 120° at the platelet edge, which also suggests that the platelets have a pseudo-hexagonal structure and high crystallinity (Fig. 1c).

Two factors have been found highly important in the synthesis of monometallic cerium layered double hydroxide compounds. One is the amount of HMT, which was used to provide alkaline environment by slowly releasing  $\text{OH}^-$  ions upon heating. The amount of HMT was 5 times higher in our case than that in conventional route previously reported; While the other is the use of  $(\text{NH}_4)_2\text{S}_2\text{O}_8$  as

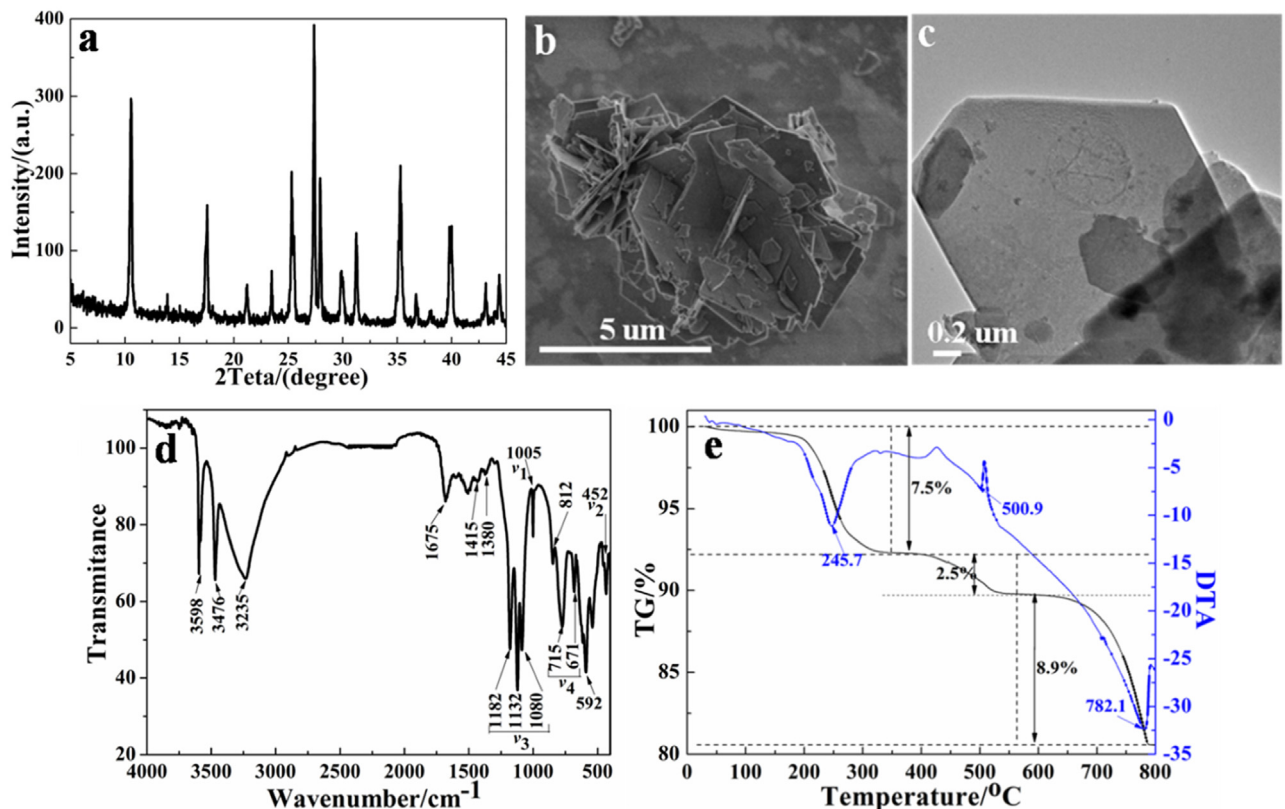


Fig. 1. XRD pattern (a), SEM (b), TEM (c), FT-IR spectrum (d) and TG-DTA profile (e) of MCe-LDH.

oxidizer whose function is to effectively convert partial  $\text{Ce}^{3+}$  into  $\text{Ce}^{4+}$ ; Without either of the two factors, the XRD pattern and SEM image of the obtained sample will be very different from those of the sample obtained in this work [17].

FT-IR spectrum of the obtained sample is displayed in Fig. 1d. All the fundamental vibration modes ( $\nu_1$ ,  $\nu_2$ ,  $\nu_3$ , and  $\nu_4$ ) observed in the spectrum can be assigned to sulfate anions in the interlayer. The  $\nu_3$  mode is split into three separate sub-peaks, which suggests that the sulfate ion ( $\text{SO}_4^{2-}$ ) has coordinated to metal ions as a *trans*-bidentate ligand through oxygen atom in the structure [23]. Other bands at around 1675, 812, and 592  $\text{cm}^{-1}$  account for the bending vibrations of water molecules coordinated to the metal ions. While three peaks around at 3500  $\text{cm}^{-1}$  are assigned to the stretching vibrations of O–H bonds, which indicates the presence of hydroxyl ions because of the metal–OH layer in the crystalline structure [19]. Two weak absorption peaks at around 1380 and 1415  $\text{cm}^{-1}$  belong to the vibration modes of  $\text{NO}_3^-$  ions and the asymmetric stretching of O– $\text{NO}_2$ , respectively [15].

The TG-DTA curve of the sample (Fig. 1e) in the temperature range of 25–800 °C shows that the compound losses its weight in three separate steps upon heating. The first weight loss of 7.5% in the temperature range of 25–340 °C is likely due to the removal of water molecules from the chemical formula. The weight loss of 2.5% in the temperature range of 340–560 °C can be attributed to the decomposition of nitrate. The final step starting from 560 °C is assigned to dehydroxylation of the hydroxide layer. No weight loss is observable at calcination temperatures higher than 800 °C, indicating the complete dehydroxylation at around 800 °C.

On the basis of the structural characteristics disclosed, it is clear that the structure of the layered Ce-hydroxide is similar to that of layered Tb-hydroxysulfate compound reported previously [19]. Ce cations are bonded by hydroxyl groups, water molecules, and oxygen atoms from the sulfate group and  $\text{NO}_3^-$  ions to form a coor-

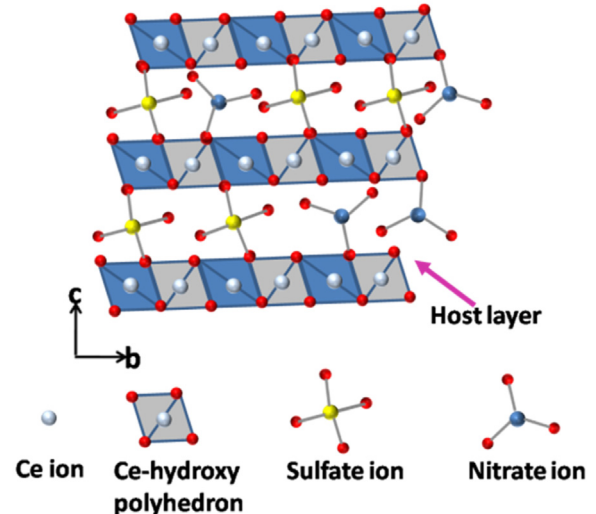


Fig. 2. Proposed ball-and-stick structure model for MCe-LDH.

dination polyhedron. One hydroxyl group is shared by three Ce cations, connecting the polyhedron to construct the host layer parallel with the a and b axes. The sulfate group bonds with two Ce cations in adjacent layers, linking them in a *trans*-bidentate configuration (Fig. 2).

### 3.2. Characterization of MCe-LDH after thermal treatments

The as-obtained monometallic cerium layered double hydroxides (MCe-LDHs) were calcined at 400 °C, 600 °C, 800 °C and 1000 °C for 6 h in air. Corresponding XRD patterns (Fig. 3A) show that the peak at about  $2\theta = 10^\circ$  has disappeared after the thermal treatment,

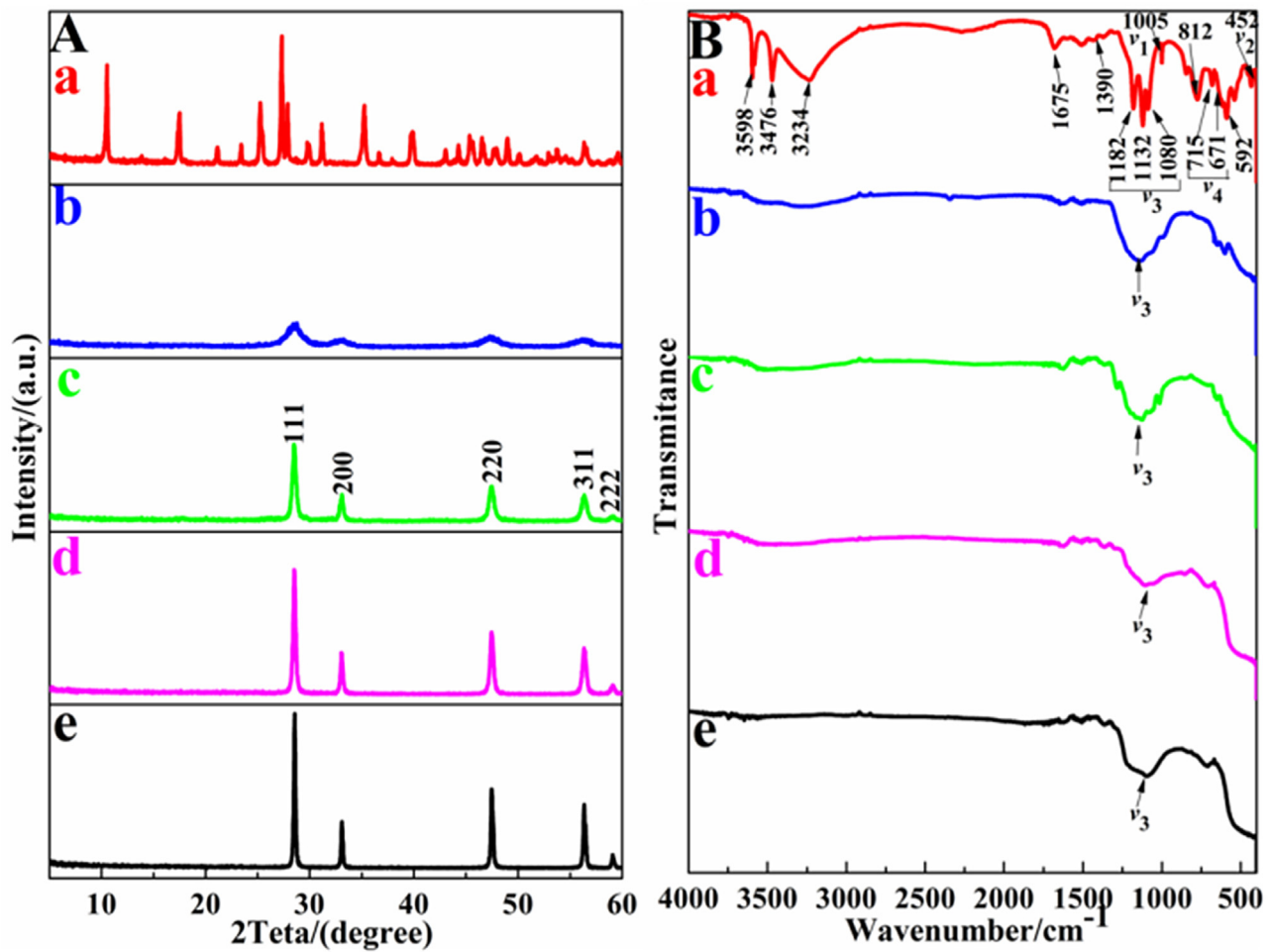


Fig. 3. XRD patterns (A) and FT-IR spectra (B) of (a) MCE-LDH and (b) MCE-LDH-400, (c) MCE-LDH-600, (d) MCE-LDH-800, (e) MCE-LDH-1000.

attributable to the removal of water molecules and the decomposition of nitrate. And they are in good agreement with the Powder Diffraction Standards data (JCPDS Card: 043-1002) being indexed to a cubic fluorite phase of  $\text{CeO}_{2-x}$ . It also can be found that the sample become better-crystallized with the increase of calcination temperature, accompanied by the dehydroxylation of hydroxide layer. According to FT-IR spectra (Fig. 3B), the triple  $\nu_3$  modes are present in the spectrum even after calcined at 1000 °C for 6 h in spite of the position shifts of peaks to a certain extent, indicating that sulfate ions in the compounds have basically kept its original configuration after the thermal treatment.

SEM images show that the products have preserved the platelet morphology after calcinations at from 400 to 800 °C, as compared to the un-calcined sample. Also, some nano-sized pores are generated on the platelets mainly because of the removal of water molecules and the decompositions of nitrate and hydroxyl from the chemical formula. With the increase of calcination temperature, the density of pores on the platelets increases as seen in Fig. 4(a–c). However, after the calcination at 1000 °C, both the platelet morphology and nanopore structure are destroyed and the particles grow much larger (Fig. 4d). As mentioned above, the dehydroxylation of the hydroxide layer and the weight loss are completed at around 800 °C, and then destructions of both the platelet morphology and pore structures follow at calcination temperatures above 800 °C. Fig. SI-2 gives the nitrogen sorption isotherms and specific surface areas of the samples after the calcination, and it can be seen that the MCE-LDH-800 has the highest surface area of 20.5 m<sup>2</sup>/g owing to the complete decomposition of hydroxyls and nitrates and

the porous structure generated. Calcination at above 800 °C has led to the porous structure collapse and much decreased surface area.

The results of XPS analyses of the samples are shown in Fig. 5. The Ce3d spectrum (Fig. 5A) between 877.5 and 920.0 eV could be deconvoluted into ten bands, which can be divided into two multiplets, labeled as  $\nu$  and  $u$ , corresponding to the spin-orbit coupling of 3d 5/2 and 3d 3/2 [24], respectively. The bands denoted as  $\nu$  ( $u$ ),  $\nu''$  ( $u''$ ), and  $\nu'''$  ( $u'''$ ) can be assigned to the photoemissions from the  $\text{Ce}^{4+}$  3d core levels respectively. Meanwhile, the signals  $\nu_0$  ( $u_0$ ) and  $\nu'$  ( $u'$ ) are ascribed to photoemissions from  $\text{Ce}^{3+}$  cations [25,26]. Therefore, it can be confirmed that the framework of the layered structure consists of mixed  $\text{Ce}^{3+}$  and  $\text{Ce}^{4+}$  oxidation states. These mixed valances of  $\text{Ce}^{3+}$  and  $\text{Ce}^{4+}$  will be responsible for the high photocatalytic activity in the  $\text{CO}_2$  reduction with  $\text{H}_2\text{O}$  vapor under irradiation, as presented in the following section.

Fig. 5B shows the O1s XPS spectra of all samples. The O1s spectrum can be deconvoluted into four bands at about 529.3, 529.8, 531.4 and 532.7 eV. The two main bands in between 529.0 and 530.0 eV can be assigned to lattice oxygen ( $\text{O}^{2-}$ ) in the metal oxides [27,28]. The one at about 531.4 eV belongs likely to chemisorbed oxygen ( $\text{O}_2^{2-}$ ). And the band of the highest binding energy (532.7 eV) is ascribed to surface oxygen by hydroxyl species ( $\text{O}_2^-$ ) on the surface [29]. The chemisorbed oxygen indicates the presence of oxygen vacancy ( $\text{V}_\text{O}$ ).

UV-vis diffuse reflectance spectra of those samples have been recorded and are shown in Fig. 6(A). It is noted that all the samples show two absorption bands at around 280 and 320 nm, which can be attributed to the absorptions of  $\text{Ce}^{3+}$  ( $\text{A}_{\text{Ce}^{3+}}$ ) and  $\text{Ce}^{4+}$  ( $\text{A}_{\text{Ce}^{4+}}$ ),

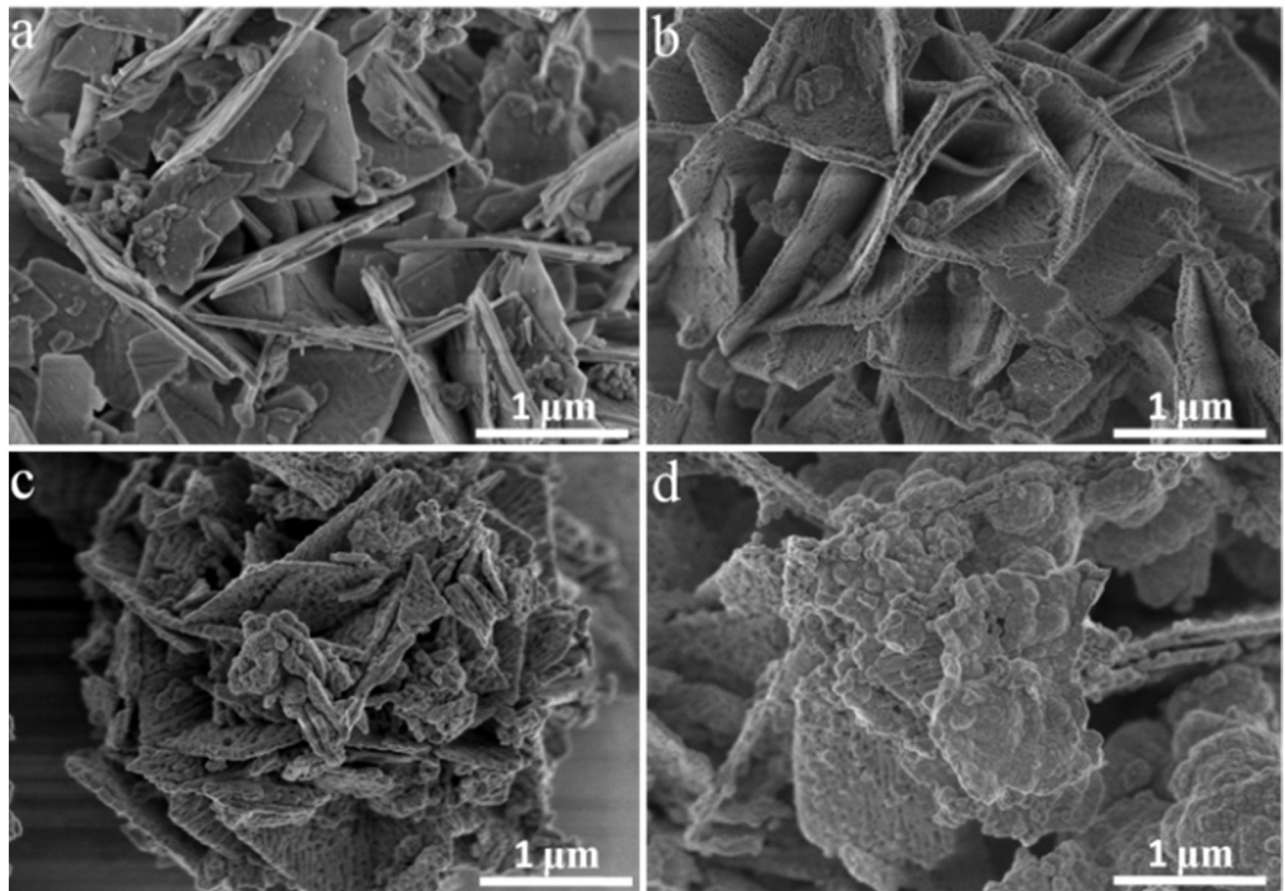


Fig. 4. SEM image of (a) MCE-LDH-400. (b) MCE-LDH-600. (c) MCE-LDH-800. (d) MCE-LDH-1000.

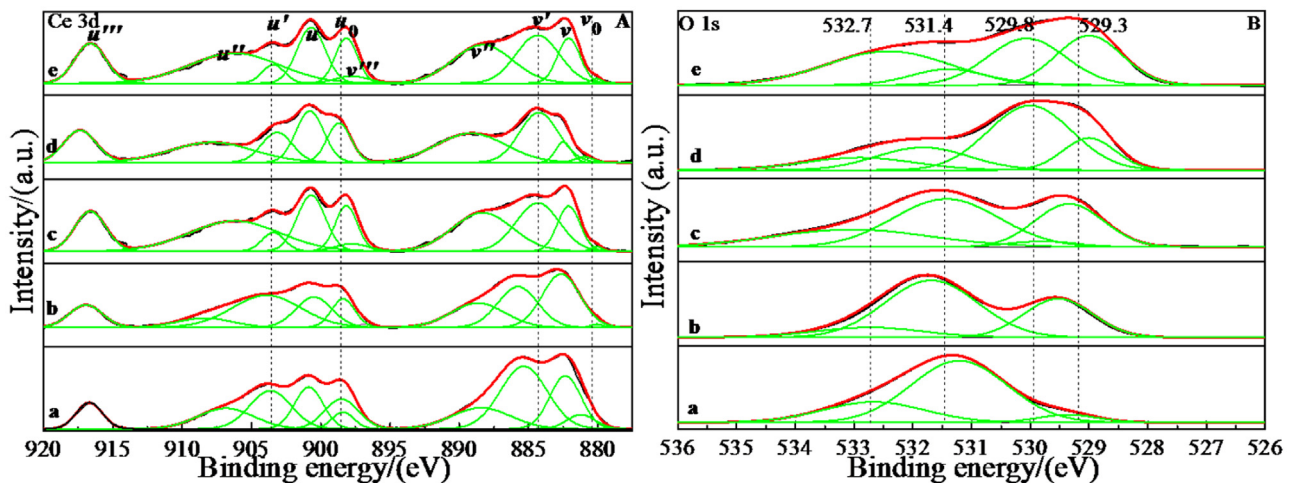


Fig. 5. Ce 3d (A) and O 1s (B) XPS spectra of (a) MCE-LDH and (b) MCE-LDH-400. (c) MCE-LDH-600. (d) MCE-LDH-800. (e) MCE-LDH-1000.

respectively [30]. Meanwhile, the change of absorbance ratio of  $A_{Ce^{3+}}/A_{Ce^{4+}}$  is closely related to the calcination temperature, as shown in Fig. 6(B). It can be observed that the absorbance ratio of  $A_{Ce^{3+}}/A_{Ce^{4+}}$  is elevated at the increased calcination temperature and reaches the maximum value for the sample calcined at 800 °C, indicating the highest concentration ratio of  $Ce^{3+}/Ce^{4+}$  in MCE-LDH-800. A slight decrease of  $A_{Ce^{3+}}/A_{Ce^{4+}}$  ratio in MCE-LDH-1000 can be observed which may be attributed to the structure destruction by the calcination at higher than 800 °C as mentioned above. The  $Ce^{3+}$  ions on the outermost surface or at the oxide–oxide interface can

act as photocatalytic active sites or hole scavengers, efficiently suppressing the surface charge recombination and extending charge carrier lifetime [26]. Thus the presence of surface  $Ce^{3+}$  ions will further promote the photocatalytic activity.

### 3.3. Photocatalytic activity of $CO_2$

The photocatalytic reduction of  $CO_2$  with  $H_2O$  vapor was performed in a gas-closed photoreactor. During the irradiation, 1 mL gas was sampled from the glass chamber every one hour for ana-

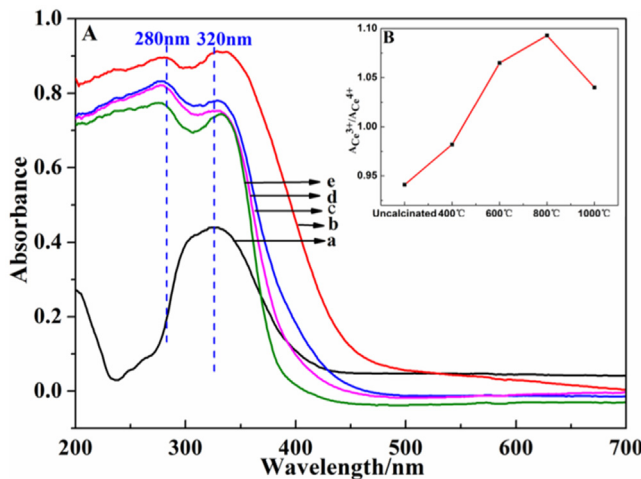


Fig. 6. UV-vis diffuse reflectance spectra (A) and  $A_{Ce^{3+}}/A_{Ce^{4+}}$  ratio (B) of (a) MCe-LDH, (b) MCe-LDH-400, (c) MCe-LDH-600, (d) MCe-LDH-800, (e) MCe-LDH-1000.

lyzing the reaction products. As a result, CO was found to be the sole product of  $CO_2$  reduction and no other carbonaceous signals were detected. Moreover  $O_2$  was also detected in large quantities in the products. Control photocatalytic experiments under identical conditions but in the absence of  $CO_2$  or light irradiation verified

that the CO and  $O_2$  were the only products, which were generated totally from the photocatalytic reduction of  $CO_2$  with  $H_2O$  vapor.

Fig. 7(A) shows the photocatalytic activities of catalysts calcined at different temperatures. The catalyst MCe-LDH-800 shows the highest activity which is in line with the above results that MCe-LDH-800 displays the highest  $A_{Ce^{3+}}/A_{Ce^{4+}}$  absorbance ratio and surface area among the calcined samples. The overall CO yield over catalyst MCe-LDH-800 is  $13.4 \mu\text{mol g}^{-1}$  in eight hours of irradiation, approximately corresponding to  $1.68 \mu\text{mol g}^{-1} \text{h}^{-1}$  on average, which is about 2.5 times that over pure m-CeO<sub>2</sub> ( $0.67 \mu\text{mol g}^{-1} \text{h}^{-1}$ ). This may be ascribed to the dominant Ce<sup>4+</sup> state in pure mesoporous CeO<sub>2</sub> as reported in the previous work [31].

Fig. 7(B) shows the production rates of CO on photocatalysts as a function of photo-illumination time. As for all catalysts, the production rates of CO firstly increased with the increase of irradiation time and then gradually decreased after reaching the maximum values, indicating a gradual deactivation of the catalytic performance. Similar results have been reported in previous studies [32–34]. The deterioration of photocatalytic activity may be caused by the diminished reactant adsorption on the catalyst surface [32,33,35] and/or the surface coverage by reaction intermediates and/or products on active sites [36,37].

Time courses of accumulative photocatalytic CO and  $O_2$  productions over the catalyst MCe-LDH-800 are presented in Fig. 7(C), which shows much more efficient production of  $O_2$  than that of

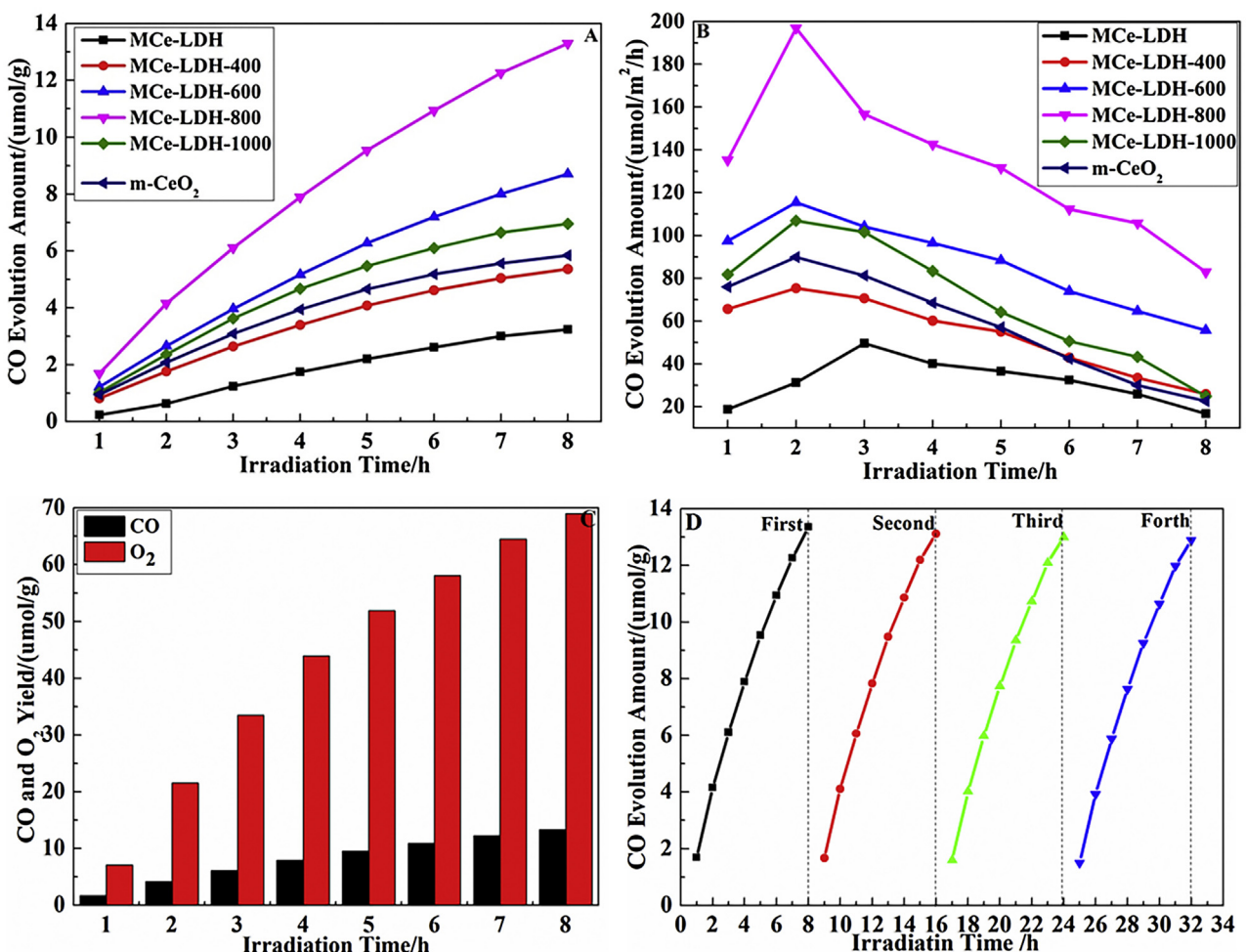
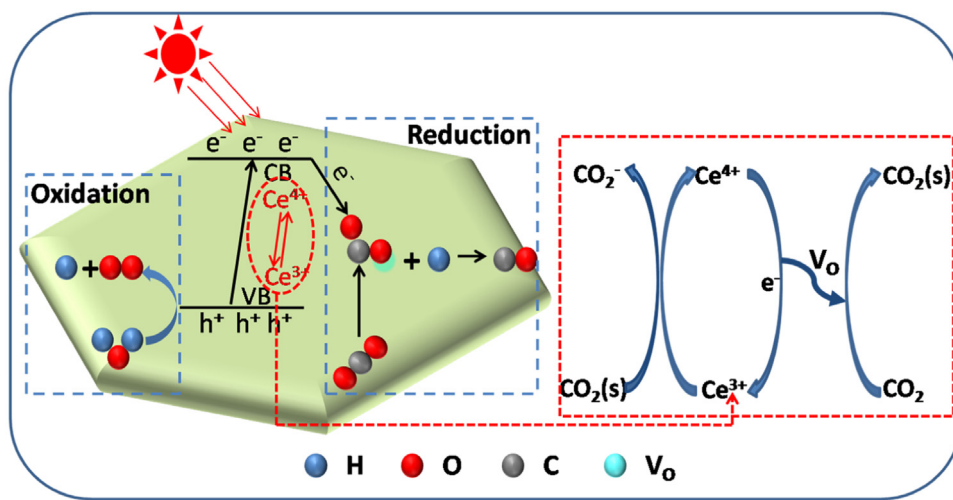


Fig. 7. (A) Time-dependent accumulative photocatalytic CO generation over different catalysts. (B) Production rate of CO on photocatalysts as a function of photo-illumination time. (C) Time courses of accumulative photocatalytic CO and  $O_2$  productions over the catalyst MCe-LDH-800. (D) Stability study of photocatalytic CO evolution over the catalyst MCe-LDH-800 under irradiation. Condition: ambient temperature, constant pressure, and 300 W Xe lamp.



**Scheme 1.** Schematic of catalytic pathway for the  $\text{CO}_2$  photoreduction with  $\text{H}_2\text{O}$  vapor.

CO. Thus it is reasonable to infer that the reaction rate was determined by CO formation and desorption [37]. Besides, a similar time course to the production of CO can be found in the production rate of  $\text{O}_2$  upon irradiation, suggesting the generation of  $\text{O}_2$  from  $\text{H}_2\text{O}$  splitting by photogenerated holes [22].

The stability of photocatalytic activity for the formation of CO over the catalyst MCE-LDH-800 was investigated via four test cycles (each for 8 h), and the result is shown in Fig. 7(D). It is clear that the catalyst maintains its high catalytic activities in four test cycles under the same reaction condition. The formation amount of CO is  $12.6 \mu\text{mol g}^{-1}$  in the forth test cycle which is about 94% that of the first run, showing a slight deactivation. In order to investigate its structure stability in the photoreduction of  $\text{CO}_2$  with  $\text{H}_2\text{O}$  vapor, we further characterized the structure of the used catalyst after photocatalytic test for 32 h by XRD and XPS analyses (Fig. SI-3) and found that there were no significant structural changes compared with the fresh sample, indicating its high structural stability. The slight deactivation may be attributed to the adsorption/coverage of the active sites by CO product or intermediates [31].

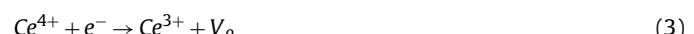
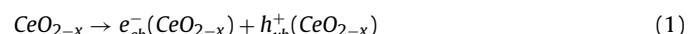
#### 3.4. Photocatalytic mechanism

As stated above, the catalyst MCE-LDH-800 showed excellent photocatalytic activity towards photoreduction of  $\text{CO}_2$  with  $\text{H}_2\text{O}$  vapor. Two factors are believed to play key roles in obtaining such an excellent photocatalytic activity. One is the  $\text{Ce}^{3+}/\text{Ce}^{4+}$  redox couple, especially the presence of  $\text{Ce}^{3+}$  on the surface of the catalysts which facilitates electron–hole separation [26]. The other is the higher surface area which provides more active sites for  $\text{CO}_2$  adsorption. Taking these factors into account, the pathway of this redox catalysis for the  $\text{CO}_2$  reduction with  $\text{H}_2\text{O}$  vapor can be outlined as shown in Scheme 1.

Firstly, electron–hole pairs are generated upon irradiation with light energy equal to or larger than the band gap energy of  $\text{CeO}_{2-x}$  (Reaction (1)). And the photo-excited electrons ( $e^-$ ) and holes ( $h^+$ ) in the lattice are separated and trapped by active sites of  $\text{CeO}_{2-x}$  to avoid recombination. Secondly,  $\text{H}_2\text{O}$  molecules are oxidized by  $h^+$  to generate  $\text{O}_2$  and  $\text{H}^+$  at the VB of  $\text{CeO}_{2-x}$  (Reaction (2)), and meanwhile  $\text{CO}_2$  molecules are reduced to CO by  $e^-$  at the CB of  $\text{CeO}_{2-x}$  under the assistance of the  $\text{H}^+$ .

As for  $\text{CO}_2$  photoreduction, there involves a reversible cycle between  $\text{Ce}^{3+}$  and  $\text{Ce}^{4+}$ , as demonstrated in XPS, i.e., both  $\text{Ce}^{3+}$  and  $\text{Ce}^{4+}$  exist on the surface of  $\text{CeO}_{2-x}$  photocatalysts. Firstly,  $\text{Ce}^{4+}$  ions will trap photo-excited electrons to form  $\text{Ce}^{3+}$  and oxygen vacancies ( $\text{V}_o$ ) (Reaction (3)) [32], meanwhile oxygen vacancies

( $\text{V}_o$ ) serve as the active sites for  $\text{CO}_2$  adsorption (Reaction (4)) as reported in previous study [38]. Secondly,  $\text{Ce}^{3+}$  ions can then react with the adsorbed  $\text{CO}_2$  ( $\text{CO}_2(s)$ ) (Reaction (5)) to regenerate  $\text{Ce}^{4+}$  [39,40] and metastable superoxide ( $\text{CO}_2^-$ ) radicals that can be further reduced to CO by  $e^-$  under the assistance of the  $\text{H}^+$  (Reaction (6)) [31,38].



#### 4. Conclusions

In conclusion, we here have successfully synthesized monometallic cerium layered double hydroxides (MCE-LDHs) for the first time through a simple approach. Such LDHs preserves its layered structure and platelet morphology after calcination at  $800^\circ\text{C}$  for 6 h, and this heat-treatment result in enhanced concentration ratio of  $\text{Ce}^{3+}/\text{Ce}^{4+}$  and highest surface area, both of which play key roles in the photocatalytic activity towards photoreduction of  $\text{CO}_2$  with  $\text{H}_2\text{O}$  vapor. The catalyst MCE-LDH-800 shows the highest photocatalytic activity and the optimum photocatalytic CO evolution rate reaches  $1.68 \mu\text{mol g}^{-1} \text{h}^{-1}$ , which is about 2.5 times that over pure mesoporous  $\text{CeO}_2$  ( $0.67 \mu\text{mol g}^{-1} \text{h}^{-1}$ ) reported in previous work. And it also maintains its high catalytic activities in repeated test cycles under the same reaction condition. Moreover, the successful synthesis of MCE-LDH provides an opportunity to develop other novel catalysts through loading functional components by intercalation, ion-exchange, or self-assembly of delaminated layer, etc.

#### Acknowledgement

This work was financially supported by National Basic Research Program of China (973 Program, 2013CB933200).

Notes and references

## Appendix A. Supplementary data

Supplementary data associated with this article can be found, in the online version, at <http://dx.doi.org/10.1016/j.apcatb.2017.03.051>.

## References

- [1] J. Kaspar, P. Fornasiero, M. Graziani, *Catal. Today* 50 (1999) 285–298.
- [2] J. Kašpar, P. Fornasiero, N. Hickey, *Catal. Today* 77 (2003) 419–449.
- [3] M.Q. Shen, M. Yang, J. Wang, J. Wen, M.-W. Zhao, W.L. Wang, *J. Phys. Chem. C* 113 (2009) 3212–3221.
- [4] S. Carrettin, P. Concepcion, A. Corma, J.M. Lopez Nieto, V.F. Puentes, *Angew. Chem. Int. Ed. Engl.* 43 (2004) 2538–2540.
- [5] B. He, Q. Zhao, Z. Zeng, X. Wang, S. Han, *J. Mater. Sci.* 50 (2015) 6339–6348.
- [6] F. Wang, R. Büchel, A. Savitsky, M. Zalibera, D. Widmann, S.E. Pratsinis, W. Lubitz, F. Schüth, *ACS Catal.* 6 (2016) 3520–3530.
- [7] Y.Y. Liu, T. Hayakawa, K. Suzuki, S. Hamakawa, *Appl. Catal. A: Gen.* 223 (2002) 137–145.
- [8] S.K. Talkhoncheh, M. Haghghi, S. Minaei, *RSC Adv.* 6 (2016) 57199–57209.
- [9] Q. Fu, A. Weber, M. Flytzani-Stephanopoulos, *Catal. Lett.* 77 (2001) 87–95.
- [10] P. Lu, B. Qiao, N. Lu, D.C. Hyun, J. Wang, M.J. Kim, J. Liu, Y. Xia, *Adv. Func. Mater.* 25 (2015) 4153–4162.
- [11] X.W. Liu, K.B. Zhou, L. Wang, B.Y. Wang, Y.D. Li, *J. Am. Chem. Soc.* 131 (2009) 3140.
- [12] C. Li, M. Wei, D.G. Evans, X. Duan, *Small* 10 (2014) 4469–4486.
- [13] Q. Wang, D. O'Hare, *Chem. Rev.* 112 (2012) 4124–4155.
- [14] F. Gandara, J. Perles, N. Snejko, M. Iglesias, B. Gomez-Lor, E. Gutierrez-Puebla, M.A. Monge, *Angew. Chem. Int. Ed. Engl.* 45 (2006) 7998–8001.
- [15] F. Geng, H. Xin, Y. Matsushita, R. Ma, M. Tanaka, F. Izumi, N. Iyi, T. Sasaki, *Chem.-Eur. J.* 14 (2008) 9255–9260.
- [16] L. Poudret, T.J. Prior, L.J. McIntyre, A.M. Fogg, *Chem. Mater.* 20 (2008) 7447–7453.
- [17] F.X. Geng, Y. Matsushita, R.Z. Mat, H. Xin, M. Tanaka, F. Izumi, N. Iyi, T. Sasaki, *J. Am. Chem. Soc.* 130 (2008) 16344–16350.
- [18] F. Geng, Y. Matsushita, R. Ma, H. Xin, M. Tanaka, N. Iyi, T. Sasaki, *Inorg. Chem.* 48 (2009) 6724–6730.
- [19] J. Liang, R. Ma, F. Geng, Y. Ebina, T. Sasaki, *Chem. Mater.* 22 (2010) 6001–6007.
- [20] X. Chang, X. Zhang, N. Chen, K. Wang, L. Kang, Z.H. Liu, *Mater. Res. Bull.* 46 (2011) 1843–1847.
- [21] P. Vialat, P. Rabu, C. Mousty, F. Leroux, *J. Power Sources* 293 (2015) 1–10.
- [22] M. Li, L. Zhang, X. Fan, Y. Zhou, M. Wu, J. Shi, *J. Mater. Chem. A* 3 (2015) 5189–5196.
- [23] S. Mizushima, I. Ichishima, I. Nakagawa, J.V. Quagliano, *J. Phys. Chem.* 59 (1955) 293–296.
- [24] Y. Wang, J. Zhao, T. Wang, Y. Li, X. Li, J. Yin, C. Wang, *J. Catal.* 337 (2016) 293–302.
- [25] X. Gao, Y. Jiang, Y. Zhong, Z. Luo, K. Cen, J. Hazard. Mater. 174 (2010) 734–739.
- [26] S. Luo, T.-D. Nguyen-Phan, A.C. Johnston-Peck, L. Barrio, S. Sallis, D.A. Arena, S. Kundu, W. Xu, L.F.J. Piper, E.A. Stach, D.E. Polyanskiy, E. Fujita, J.A. Rodriguez, S.D. Senanayake, *J. Phys. Chem. C* (2015), 150127101000001.
- [27] S. Yang, W. Zhu, Z. Jiang, Z. Chen, J. Wang, *Appl. Surf. Sci.* 252 (2006) 8499–8505.
- [28] Z. Zhang, Z. Zhou, S. Nie, H. Wang, H. Peng, G. Li, K. Chen, *J. Power Sources* 267 (2014) 388–393.
- [29] J.C. Dupin, D. Gonbeau, P. Vinatier, A. Levasseur, *Phys. Chem. Chem. Phys.* 2 (2000) 1319–1324.
- [30] M. Lu, Y. Zhang, Y. Wang, M. Jiang, X. Yao, *ACS Appl. Mater. Interfaces* 8 (2016) 23580–23590.
- [31] M. Li, L. Zhang, M. Wu, Y. Du, X. Fan, M. Wang, L. Zhang, Q. Kong, J. Shi, *Nano Energy* 19 (2016) 145–155.
- [32] Y. Li, W.-N. Wang, Z. Zhan, M.-H. Woo, C.-Y. Wu, P. Biswas, *Appl. Catal. B: Environ.* 100 (2010) 386–392.
- [33] W.N. Wang, W.J. An, B. Ramalingam, S. Mukherjee, D.M. Niedzwiedzki, S. Gangopadhyay, P. Biswas, *J. Am. Chem. Soc.* 134 (2012) 11276–11281.
- [34] C. Zhao, L. Liu, Q. Zhang, J. Wang, Y. Li, *Catal. Sci. Technol.* 2 (2012) 2558.
- [35] N. Sasirekha, S. Basha, K. Shanthi, *Appl. Catal. B: Environ.* 62 (2006) 169–180.
- [36] I.H. Tseng, W.C. Chang, J.C.S. Wu, *Appl. Catal. B: Environ.* 37 (2002) 37–48.
- [37] M. Li, L. Zhang, X. Fan, M. Wu, M. Wang, R. Cheng, L. Zhang, H. Yao, J. Shi, *Appl. Catal. B: Environ.* 201 (2017) 629–635.
- [38] Y.X. Pan, Z.Q. Sun, H.-P. Cong, Y.L. Men, S. Xin, J. Song, S.H. Yu, *Nano Res.* 9 (2016) 1689–1700.
- [39] Y.H. Xu, Z.X. Zeng, *J. Mol. Catal. A: Chem.* 279 (2008) 77–81.
- [40] L. Liu, C. Zhao, Y. Li, *J. Phys. Chem. C* 116 (2012) 7904–7912.